# Residual stress fields in sol-gel-derived thin TiO2 layers

Teeuw, D.H.J.; Haas, M. de; Hosson, J.Th.M. De

*Published in:*
Journal of Materials Research

Journal of
MATERIALS RESEARCH



# Residual stress fields in sol-gel-derived thin $TiO_2$ layers

D. H. J. Teeuw, M. de Haas, and J. Th. M. De Hosson[a)]
*Laboratory of Applied Physics, Materials Science Center and Netherlands Institute for Metals Research, University of Groningen, Nijenborgh 4, 9747 AG Groningen, The Netherlands*

(Received 11 March 1998; accepted 19 November 1998)

This paper discusses the induction of residual stresses during the curing process of thin titania layers, which are derived using a sol-gel process. During this process, stresses may build up in the spinning stage, the drying stage, and the consolidation stage. The magnitude and character of these stresses depend heavily on the morphology of the layers in the various stages and the processing conditions. Dried layers are densified using two different processes, conventional furnace heating and laser heating. X-ray analysis and scanning electron microscopy are used as tools to study crystallization, grain growth, phase transformation, and the evolution of residual stress fields in the thin titania layers. Through an extensive study of the residual stress state in the layers, more insight is gained in the evolution of stresses during the curing process of sol-gel-derived thin titania layers.

## I. INTRODUCTION

Ceramic materials are widely used for their superb performance in applications where other classes of material may fail. Possible applications are circumstances where materials have to withstand high temperatures, corrosion environments, and severe wear. Besides coatings, complex millimeter-sized 3D ceramic/metal products can be manufactured. A conventional method to produce ceramic foils is based on slipcasting. Another method for the production of coatings is wet-chemical processing, also called sol-gel processing. Sol-gel processing may be defined as the preparation of ceramic materials by preparation of a sol, gelation of the sol, removal of the solvent, and further heat treatments. Here, the sols are produced starting from alkoxides. Sol-gel coatings can be used in many more applications than for protective matters only, such as in the optical and electronic. The problem of homogeneity, often encountered in the processing of powders, is absent in the sol-gel preparation technique because no comminution is required. Moreover, the processing temperatures can be significantly reduced, and combining different coating liquids (hybrid systems) is easy. This latter aspect offers a great deal of freedom to fabricate coatings with different properties. Finally, the introduction of organic or conductive additives into the product is possible.

The densification of sol-gel layers takes place by mass transport from particles to the interconnecting points between these particles, thereby reducing total porosity. Mass transport may take place through diffusion processes or viscous flow. The driving force results from minimization of the surface energy. After spinning and evaporation, the layers are usually densified by further heat treatments and the objective of this paper is to report on the residual stress state that results after the complete thermal cycle of preparation, drying, i.e., after heating up and cooling down. The research presented in this paper concentrates on the densification of sol-gel-derived thin nanotitania coatings by laser radiation and by furnace treatment. Deposition of the film is done by means of spin coating. This paper primarily aims at studying the residual stress states which evolved during the production process for the titania coatings. Tensile stresses evolve in the layers during the spinning and drying stage. Due to capillary forces as a result of the evaporation of liquids in the solid network, tensile stresses evolve in the layer. The question is what is the residual stress state left after the additional post-heat treatments.

### A. Materials

The sols are produced starting from alkoxides as the precursor, here a tetraethylorthotitanate precursor, $Ti(OC_2H_5)_4$ or TEOTi, is used.[1] This precursor will result in $TiO_2$ after deposition, gelation, and condensation. The sols are deposited on fused silica substrates by means of spin coating, as schematically depicted in Fig. 1.[2]

After spinning and evaporation, the layers are densified in a furnace or laser treatment. During furnace densification, the sample is placed in a furnace and cured in air at temperature $T$ for a time $t$. For laser curing, the power density $P$ and interaction time $\tau$ are determined by[3]

$$P = \frac{I}{\pi\left(\frac{x}{2}\right)^2} \qquad \tau = \frac{x}{v}\,. \tag{1}$$

a)e-mail: hossonj@phys.rug.nl

 

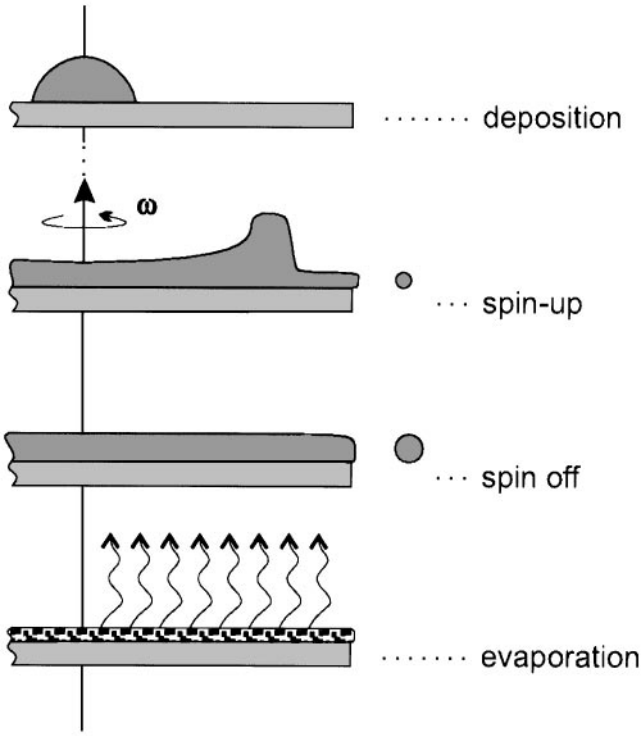


FIG. 1. Various stages in the spin process of the thin titania layers.

Here $x$ is the diameter, $I$ the intensity of the laser beam, and $v$ its scanning velocity. To investigate the impact which the several parameters have on the final properties of the layer, furnace as well as laser-cured specimen are studied using x-ray diffraction. Especially, residual stress analysis and phase analysis are performed on a set of differently processed sol-gel-derived thin $TiO_2$ layers.

### B. Experimental

X-ray diffractograms are recorded for furnace- as well as laser-cured specimens using the $\theta$-$2\theta$ goniometer setup. The experiments are performed using a Philips PW1820 goniometer. A divergence slit of $1/6°$ and soller slits are present at the primary optics side; at the secondary optics side a receiving slit of 0.2 mm, an antiscatter slit of $1/2°$, soller slits, and a monochromator are installed. Since the diffraction yield of the thin layers is low, no reflections are found for large values $2\theta$. To study crystallization processes and phase transformations in the nanocrystalline material, diffractograms are recorded over a $2\theta$ range in which the main reflections for crystalline $TiO_2$ are expected, from $2\theta = 21.0°$ to $2\theta = 29.0°$.

Residual stress measurements are performed on a Philips X'Pert PW 3040 x-ray diffractometer. The diffractometer is equipped with a $\psi$-goniometer, PW 3050, with MRD-Cradle. In order to employ the $\psi$-tilting properly, the x-ray tube is mounted to deliver a point-focus beam. A crossed slit collimator is used to adjust the horizontal and vertical divergence of the beam. At the secondary optics side a wide receiving slit, 0.2 mm, is installed to maximize diffraction yield. The generator operates at 40 kV, 50 mA, and Cu $K_\alpha$ radiation is used. The measurements are performed using positive as well as negative $\psi$-tilting for different orientations $\phi$ of the specimen. The aim of this extensive set of orientations is to check whether the residual stress state in the material is triaxial. If no triaxial stress state is present, it would suffice to measure only positive or negative $\psi$-angles for one orientation $\phi$ and analyze the measurements using the $\sin^2\psi$ method.[4]

$$\begin{aligned}\epsilon_{33,L,\phi\psi} = {} & \epsilon_{11}\cos^2\phi\sin^2\psi + \epsilon_{12}\sin 2\phi\sin^2\psi \\ & + \epsilon_{22}\sin^2\phi\sin^2\psi + \epsilon_{33}\cos^2\psi \\ & + \epsilon_{13}\cos\phi\sin 2\psi + \epsilon_{23}\sin\phi\sin 2\psi\,. \qquad (2)\end{aligned}$$

Equation (2) describes the dependence of the measured strain in crystallites with orientation $\phi$, $\psi$ on the existing macrostrain in the specimen.

## II. EXPERIMENTAL RESULTS

### A. Crystallization and phase analysis

In Fig. 2 the recorded diffractograms for the furnace-cured specimen are displayed. From the recorded diffractograms, several properties of the layers may be observed. The diffractogram of the 300 °C cured specimen does not show any Bragg reflections. This indicates that the material does not contain crystallites which are in a suitable position for diffraction; e.g., they do not satisfy the Bragg law for diffraction. This may lead to two explanations. Either the layer is highly textured and the reflections cannot be measured using the $\theta$-$2\theta$ setup, or the layer is amorphous. Texture will be discussed in the last section to draw accurate conclusions concerning the morphology of the layer, the

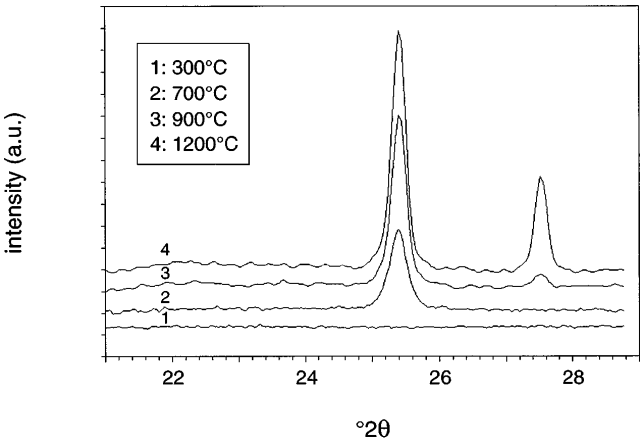


FIG. 2. Determined x-ray diffractograms for the furnace-cured thin $TiO_2$ layers. From the displayed diffractograms information on crystallization, grain growth, and phase transformation may be obtained.

remaining specimen will be examined first. If the curing temperature is increased, a reflection emerges as may be observed for the 700 °C cured specimen. This emerging reflection indicates that, in contrast to the 300 °C cured specimen, there are crystallites in a preferred orientation for diffraction. The $2\theta$ value of this reflection, 25.28°, can be transformed using the Bragg equation to a lattice spacing of $d = 3.52 \times 10^{-1}$ nm, which corresponds to the lattice distance of the {101} planes of anatase, the low temperature tetragonal phase of $TiO_2$.[5,6]

Upon further increasing the curing temperature to 900 °C, the anatase reflection at 25.28° $2\theta$ becomes more pronounced, indicating that the layer becomes more crystalline. As an additional effect of the increased curing temperature, a second reflection is observed at 27.44° $2\theta$. This reflection is due to a lattice set with spacing $d = 3.247 \times 10^{-1}$ nm and corresponds to the {110} planes of the rutile phase of $TiO_2$. This means that the layer is partly transformed from the low temperature phase, anatase to the high temperature rutile phase. For bulk materials this transition is expected around 750 °C.[7,8]

Finally, a diffractogram of a specimen cured at 1200 °C is displayed. The anatase reflection has increased even further. The rutile reflection has also become very distinct. Together, it can be concluded that the layer has become even more crystalline and that more crystallites are transformed from the anatase phase to the rutile phase.

The recorded diffractograms do not only provide information concerning the phase of the material. From the width of the determined line profiles more information may be gained, and the average crystallite size can be determined using the Scherrer equation[9]

$$D = \frac{K\lambda}{B\cos\theta_B}, \tag{3}$$

where $K$ is a factor $\sim 0.9$–$1.0$, $\lambda$ the wavelength of the radiation used, and $B$ the broadening of the profile. The broadening $B$ has to be corrected for instrumental broadening due to slit sizes and x-ray source characteristics. To measure the instrumental broadening, a reference diffractogram is recorded from a standard specimen. This specimen should not broaden the line profiles; therefore, the crystallite size should be larger than $\sim 1.0$ $\mu$m and the grains should not be strained. Silicon powder with grain size of $\sim 5.0$ $\mu$m may be used as a standard. Using similar experimental settings as for the recorded diffractograms of the $TiO_2$ layers, the {111} reflection of silicon at 28.442° $2\theta$ is recorded. From this line profile, the determined instrumental line broadening is $B = 0.09°$ $2\theta$. Using the x-ray line broadening as determined from the diffractograms in Fig. 2, an estimate for the average crystal size in the layers is given in Table I.

Low-voltage high resolution scanning electron microscopy is used to measure the grain sizes in an alternative way. The linear intercept method[10] delivers values for the average grain sizes in the samples. This method makes use of a line of known length $l$ drawn over the surface of the samples. Every intersection of this line with a grain boundary is counted. When sufficient intersections are determined, the average grain radius $R$ is a direct measure from the number of intersections $(N)$ per total line length $(L)$, provided that sufficient, $\sim 450$, intersections are determined.[11,12]

$$R = \frac{3L}{4N}. \tag{4}$$

The measurements are performed on a set of micrographs, typically represented by Fig. 3, where *a*, *b*, and *c* represent micrographs of specimens treated at 700, 900, and 1200 °C, respectively. The results of the measurements are listed in Table II.

The values determined using the linear intercept method correspond well to the values derived using the x-ray line broadening experiments, leaving the x-ray

TABLE I. Average crystallite sizes furnace-cured $TiO_2$ specimen.

| Temperature (°C) | Broadening (°$2\theta$) | Average grain radius, $D/2$, Eq. (3) (nm) |
|---|---|---|
| 300 | ... | ... |
| 700 | 0.241 | 26.9 ± 0.1 |
| 900 | 0.172 | 49.7 ± 0.1 |
| 1200 | 0.137 | 86.7 ± 0.1 |

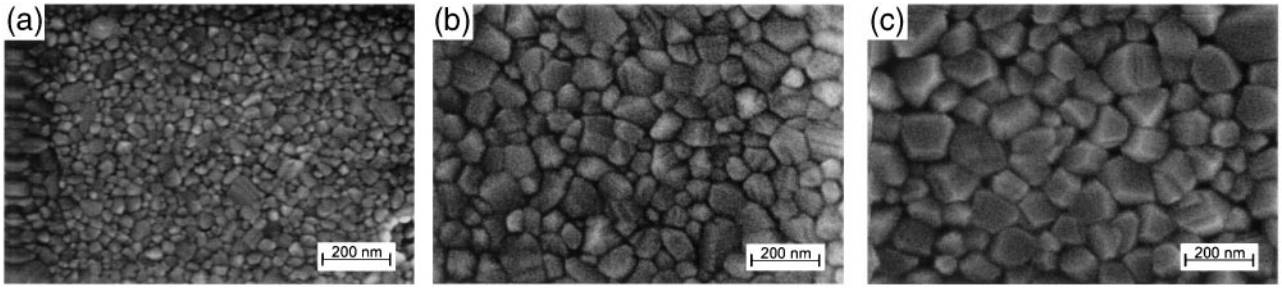


FIG. 3. (a–c) Micrographs of 700, 900, and 1200 °C furnace-cured $TiO_2$ specimens.

TABLE II. Grain sizes furnace-cured $TiO_2$.

| Heat treatment (°C) 30 min hold | Average grain radius, *R*, Eq. (4) (nm) |
|---|---|
| 300 | −/− |
| 700 | 24.2 ± 0.1 |
| 900 | 50.1 ± 0.1 |
| 1200 | 89.7 ± 0.1 |

TABLE III. Average crystallite sizes laser-cured specimen.

| Laser ($kW/mm^2$, mm/s) | Broadening (°2$\theta$) | Average grain size (nm) |
|---|---|---|
| 35, 43 | 0.185 | 85.7 ± 0.1 |
| 50, 119 | 0.215 | 65.1 ± 0.1 |
| 55, 136 | 0.190 | 81.4 ± 0.1 |

experiments an accurate method to determine average grain sizes in these layers.

To investigate the crystalline properties and the phase of the laser-cured specimen, diffractograms are recorded using similar settings which were used for the furnace-cured specimen. In Fig. 4 three diffractograms are depicted for laser-cured specimen with different curing parameters.

The three diffractograms exhibit similar behavior, indicating that the phase and structure of the layers are comparable. In contrast to the furnace-cured specimen, there is no evolution in crystallization and the transformation from anatase to rutile is in general not observed, and only faintly for the specimen cured using laser parameters 55 $kW/mm^2$, 136 mm/s. Overall, the diffraction yield is small, compared to the furnace-cured specimen. To perform x-ray residual stress measurements accurately, the intensity of the reflection under investigation has to be ~10 times the background. The intensity drops heavily upon tilting of the specimen, which makes it not possible to perform residual stress measurements on these layers.

To get some insight in the morphology of the laser-cured layers, the width of the profiles is determined in order to derive a value for the average crystallite sizes in the laser-cured layers. The derived values are listed in Table III.

The average crystallite sizes do not deviate to a large extent, indicating that grain growth is not affected by the laser settings used in these experiments.

### B. X-ray residual stress measurements

X-ray residual stress measurements are performed on the furnace-cured $TiO_2$ specimens. First the 1200 °C specimen is studied. The anatase reflection at 25.28° $2\theta$ proved in the phase analysis experiments to exhibit an intensity versus background ratio which is large enough for x-ray residual stress analysis to be performed. The position of the Bragg reflection is determined as a function of crystallite orientations $\phi$, $\psi$. For three azimuthal angles, $\phi = 0°$, 45°, and 90°, the tilt angle $\psi$ is varied from −45° to 45° in steps $\Delta \sin^2 \psi = 0.12$. The results of the measurements are displayed in Fig. 5. For the different azimuthal angles $\phi$, an offset is added to the measured values for clarity.

From the measurements it is seen that the dependence of the lattice spacing upon the crystallite orientation is linear, which is expected for linear elastic isotropic media. For the larger $\psi$ values, however, the lattice spacings measured for positive and negative $\psi$ values do show some deviations. This may be due to the existence of shear components in the strain tensor. From Eq. (2) it is seen that if $\epsilon_{13}$ and $\epsilon_{23}$ are nonzero,

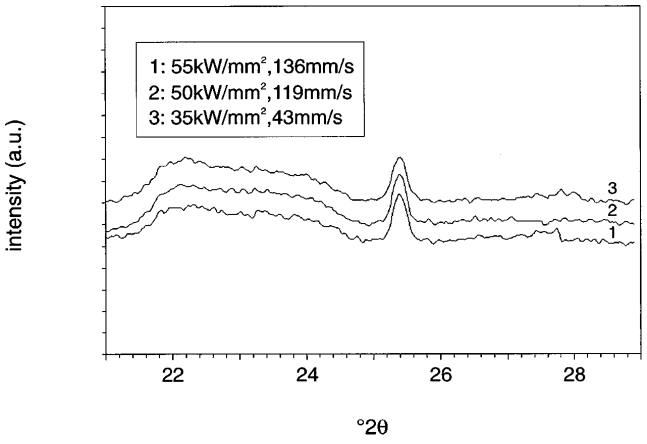


FIG. 4. Determined x-ray diffractograms for the laser cured thin $TiO_2$ layers.

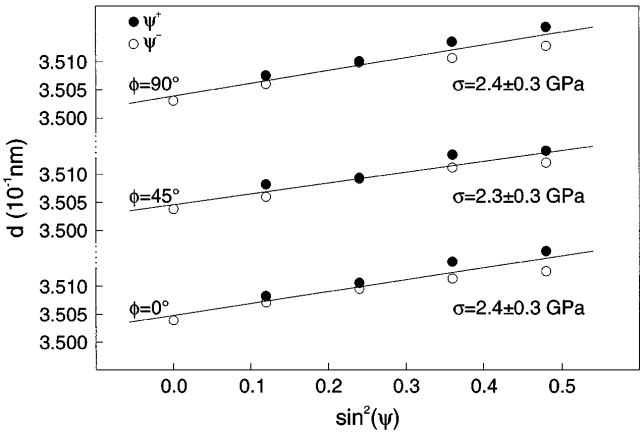


FIG. 5. Determined lattice spacings for the 1200 °C furnace cured specimen as a function of specimen tilt $\psi$ in azimuthal orientations $\phi = 0$, 45, and 90°.

an extra contribution to the measured strain is expected, which differs for positive and negative values of $\psi$ due to the term $\sin(2\psi)$. To investigate whether the stress state in the layer is triaxial, a procedure is followed which enables the separation of the contributions from the several strain components on the measured lattice strains.[13] If for an orientation $\phi$ the average lattice strain $\epsilon_{\text{avg}}$ is calculated from the measured values $d^+$ and $d^-$, the following expression may be derived

$$\begin{aligned}\epsilon_{\text{avg}} &= \frac{d_{\phi\psi^+} + d_{\phi\psi^-}}{2d_0} - 1 \\ &= \frac{1}{2}\left\{\frac{d_{\phi\psi^+} - d_0}{d_0} + \frac{d_{\phi\psi^-} - d_0}{d_0}\right\} \\ &= \{\epsilon_{11}\cos^2\phi + \epsilon_{12}\sin 2\phi + \epsilon_{22}\sin^2\phi - \epsilon_{33}\} \\ &\quad \times \sin^2\psi + \epsilon_{33}\,. \end{aligned} \tag{5}$$

From Eq. (5) it is seen that plotting $\epsilon_{\text{avg}}$ as a function of $\sin^2\psi$ delivers a straight line. Measuring $\epsilon_{\text{avg}}$ for azimuthal angles $\phi = 0°$, 45°, 90° yields a set of equations from which the strain components $\epsilon_{11}, \epsilon_{12}, \epsilon_{22}, \epsilon_{33}$ may be determined. A similar procedure may be followed to determine the shear strains $\epsilon_{13}$ and $\epsilon_{23}$. By taking the difference between the measured lattice strains for positive and negative $\psi$ values, an expression may be derived which correlates the shear strains to the crystallite orientation $\phi$.

$$\begin{aligned}\epsilon_{\text{dif}} &= \frac{d_{\phi\psi^+} - d_{\phi\psi^-}}{2d_0} \\ &= \{\epsilon_{13}\cos\phi + \epsilon_{23}\sin\phi\}\sin|2\psi|\,. \end{aligned} \tag{6}$$

Plotting $\epsilon_{\text{dif}}$ against $\sin|2\psi|$ for azimuthal angles $\phi = 0°$, 90° delivers the shear strains $\epsilon_{13}$ and $\epsilon_{23}$ from the gradient of the derived line. In Fig. 6 the dependence of $\epsilon_{\text{avg}}$ on $\sin^2\psi$ and the dependence of $\epsilon_{\text{dif}}$ on $\sin|2\psi|$ are plotted, respectively, for the three different azimuthal orientations used.

From Fig. 6 the strain components are determined as:

$$\text{measured strains}: \begin{pmatrix} 5.8 & -0.8 & 0.08 \\ \cdots & 6.1 & 0.6 \\ \cdots & \cdots & 0.3 \end{pmatrix} \times 10^{-3}.$$

The derived values for the strain components indicate that a biaxial strain field exists in the layer. The values for $\epsilon_{11}$ and $\epsilon_{22}$ are overall $\sim 10$ times larger than the other strain components, where the measured shear strain components $\epsilon_{13}$ and $\epsilon_{23}$ are small compared to the principal strains $\epsilon_{11}$ and $\epsilon_{22}$. Assuming that the material is isotropic in its elastic properties, the presence of a biaxial strain state indicates that the stress state is also biaxial. Therefore, application of the $\sin^2\psi$ method is justified to measure residual stresses in these layers. For the three azimuthal directions the stresses

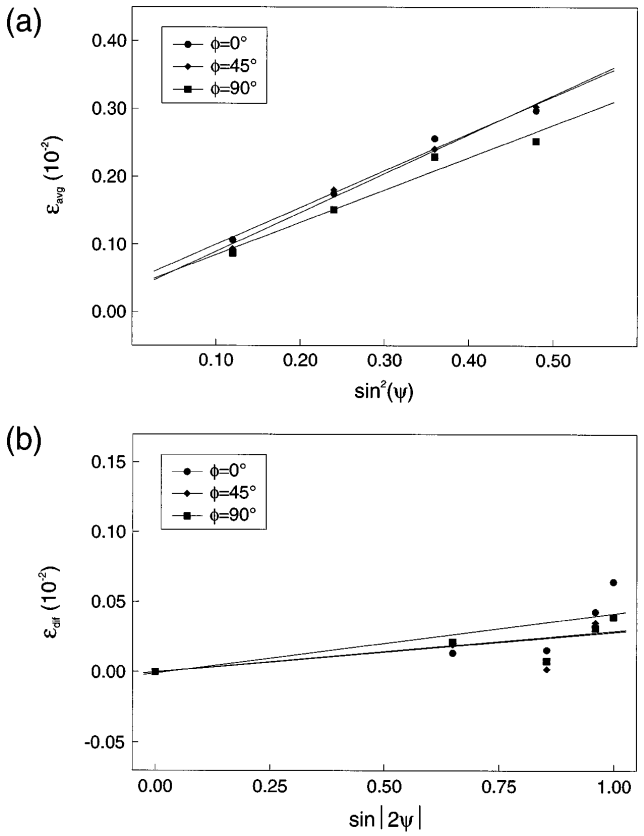


FIG. 6. Determination of triaxial strain. (a) Evaluation of the average lattice spacing, as defined by Eq. (5), as a function of specimen tilt $\psi$. (b) Evaluation of the differential lattice spacing, as defined by Eq. (6), as a function of specimen tilt $\psi$.

TABLE IV. Measured stress 1200° specimen.

| $\phi$ (°) | $\sigma_\phi$ (GPa) |
|---|---|
| 0 | 2.4 ± 0.3 |
| 45 | 2.3 ± 0.3 |
| 90 | 2.4 ± 0.3 |

are determined as listed in Table IV; in the analysis, the material properties of $TiO_2$ are used according to $E = 410$ GPa, $\nu = 0.19$.

The values determined for the orientations $\phi$ are comparable within the error margins, indicating that the stress state is biaxial and, from Eq. (2), it also follows that $\sigma_{11} = \sigma_{22}$, determining the value $\sigma_\phi$. Consequently, an averaged residual stress value is derived for the 1200 °C specimen, $\sigma_{\text{res}} = 2.4 \pm 0.2$ GPa.

Similar experiments are conducted for the 700 °C and the 900 °C specimen. The measurements are again averaged, since no discrepancies are found between the measured stresses as a function of azimuthal orientation

TABLE V. Experimentally derived stresses in layers.

| Curing temperature (°C) | $\sigma_{res}$ (GPa) |
|---|---|
| 700 | 1.4 ± 0.2 |
| 900 | 2.0 ± 0.1 |
| 1200 | 2.4 ± 0.2 |

$\phi$. The eventually determined residual stress states in the layers are listed in Table V.

## III. DISCUSSION AND CONCLUSIONS

X-ray residual stress measurements are performed on the $TiO_2$ layers, and a relevant point of discussion is whether the basic requirements necessary to the performance of x-ray residual stress measurement are met. The material must be polycrystalline in order to perform stress analysis using linear elasticity theory. If the material is monocrystalline, there will only be one orientation $\psi$ for which the Bragg law is satisfied and x-ray residual stress analysis is not possible. If the material exhibits preferred orientation, i.e., the material is textured, x-ray residual stress measurements also may become a problem. When a material is textured to a large extent, Bragg reflections will decrease upon tilting the specimen from its preferred orientation, as for the case of monocrystalline materials. Additionally, texture in a polycrystalline material may cause the material to become anisotropic in its linear properties. Especially for materials which exhibit larger anisotropy in Young's modulus, this may give rise to problems. For a polycrystalline material, which is considered to be isotropic in its macroscopic elastic behavior, it is not a problem, provided that the analysis uses $\{hkl\}$ plane specific x-ray elastic constants. For highly textured materials, it may become questionable, because Hooke's law no longer applies. To check whether the materials were textured, the diffraction yield was measured for all orientations $\phi$, $\psi$ of crystallites in the specimen. This is done by placing the detector at the $2\theta$ reflection of interest. Subsequently, the specimen is tilted over an angle $\psi$. After measuring the diffraction yield as described for a specific tilt angle $\psi$, all angles $\phi$ are measured. Because tilting a specimen will cause defocus errors in the measured intensity, the measurements are corrected according to calculated defocus patterns. The data can be plotted in a contour plot with axes $\phi$ and $\psi$. If any preferred orientation is present in the specimen, it will show as poles in the contour plots. The measurements were performed on the same Philips X'Pert MRD system, but operating in a texture analysis mode. The x-ray source is mounted to deliver a point focus beam. At the primary optics side a cross slit collimator is installed; at the secondary optics side a wide receiving slit, 0.2 mm, is installed. No soller slits and no filters are used. For the 1200 °C specimen, a contour plot is measured for the {101} anatase reflection at $2\theta = 25.28°$. The tilt angle $\psi$ is varied from 0° to 45° and $\phi$ ranges from 0° to 360°. At every crystal orientation, the diffraction yield is measured for 5 s. Afterward, corrections are made for defocusing effects. The determined contour plot is displayed in Fig. 7(a). The measurements indicate that there is no distinct preferred orientation present. For $\psi$ tilts ranging from $\sim 10–30°$, the intensity measured is mostly constant, with some areas with increased diffraction yield. For specific $\phi$ orientations, 0°, 90°, 180°, 270°, a slight increase in intensity can be observed, indicating that more crystals are oriented in this orientation. For the 900 °C specimen a contour plot is measured using a similar procedure to the 1200 °C specimen. The result is displayed in Fig. 7(b). The contour plot exhibits features comparable to the contour plot for the 1200 °C specimen. Intensity as a function of $\psi$ is constant over a large range of $\psi$ values. An increase in diffraction yield is

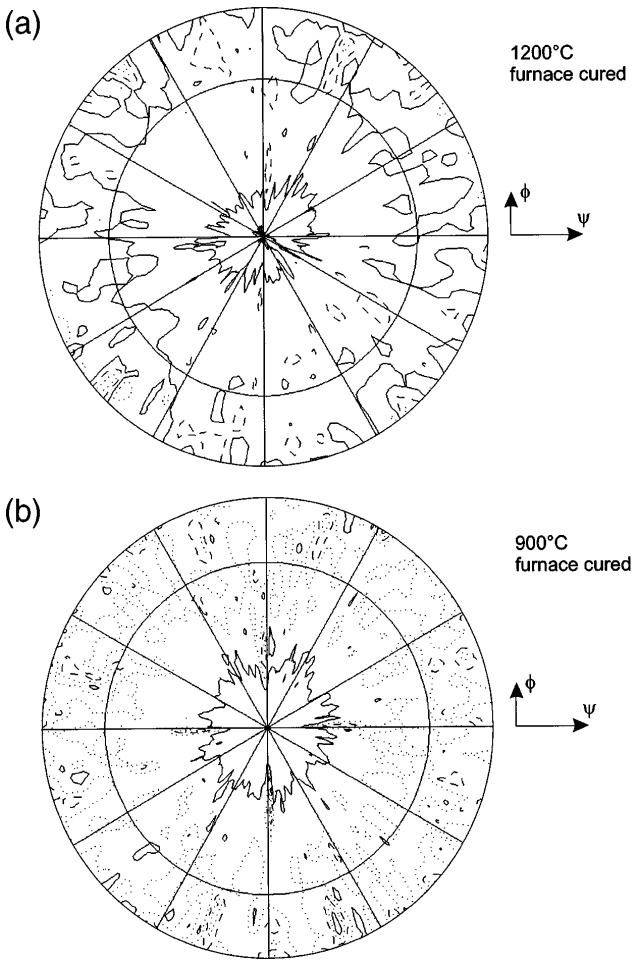


FIG. 7. Pole figures for the (a) 1200 °C and (b) 900 °C specimen. The measured intensity of the $2\theta = 25.28°$ reflection is measured as a function of the tilt angle $\psi$, plotted radially, and azimuthal angle $\phi$.

again observed, as for the 1200 °C specimen, for specific crystallite orientations $\phi = 0°$, 90°, 180°, 270°. The magnitude of these poles in the contour plots is slightly larger for the 900 °C specimen than for the 1200 °C specimen. The 900 °C specimen was cured twice as long, 60 min, versus 30 min for the 1200 °C specimen, which may be an explanation for the more pronounced preferred orientation in this specimen.

From the contour plots it is concluded that x-ray diffraction can be used to measure residual stress fields in these specimens. The layers contain randomly oriented crystallites, which is a requirement for application of x-ray residual stress analysis.

The thin $TiO_2$ layers proved to exhibit large differences in morphology, structure, and residual stress state between dissimilar curing processes. The question is whether the drying process that proceeds further curing treatments already sets the stress level right from the start. Upon drying the layer the rate of evaporation of liquid, $V_L$, must equal the flux of liquid, $J_L$, from the solid porous network to the surface. $J_L$ is determined by the permeability of the film $(D)$, the viscosity of the liquid $\eta_L$, and the pressure gradient in the liquid. This gradient causes the liquid-vapor interface to remain at the surface of the drying film and to compress the network in the film. The liquid covering the solid phase will be in tension. The tension is balanced by compressive stresses which tend to suck the network under the surface of the liquid. The permeability in turn depends strongly upon the average capillary size $\delta$ ($D \approx \delta^4$),[2] and hence upon the pore size in the solid network. Because of the very small pore sizes of the solid network in the drying film, the permeability is relatively low with respect to ordinary bulk ceramics. As a consequence of this low permeability, very steep pressure gradients may arise, even for modest drying rates. The steeper, the greater the difference in shrinkage rate between the exterior and the interior of the network, and the more likely the film is to fracture. From the pressure gradient, a relation for the maximum tensile stress which occurs at the surface of the film can be approximated.[2] This relation also includes the thickness of the film $L$:

$$\sigma \approx \frac{L \eta_L \dot{V}_L}{3D} . \tag{7}$$

Equation (7) shows that high tensile stresses are expected for thick films, or when drying at high evaporation rates, and for networks which have low permeability. The average pore diameter in the layer will decrease after drying. This decreasing pore size distribution will result in a decrease in permeability of the layer, and hence increasing the stress rate in the layer. These stresses due to capillary forces are present in the dried starting material of a certain thickness governed by evaporation processes of the volatiles. The densification of titania films in particular is strongly affected by the internal atmosphere (organic alkyl groups) and heating rate.[14,15] At higher temperatures as in our experiments these stresses due to capillary forces will be reduced substantially by the dynamic character of the densification/sintering process and probably also by creep mechanism.

For the various curing temperatures an evolution in phase is observed. The 300 °C specimen is still amorphous after the curing process. Since this specimen does not exhibit any Bragg reflection, due to the amorphous state of the layer, an average crystallite size cannot be determined from line broadening experiments. For the same reason, x-ray residual stress analyses are not performed on this specimen.

Curing the layer at 700 °C results in crystallization of the $TiO_2$ layer in the anatase form. This crystallization typically results in a large compressive stress. The formation of grains in the layer is accompanied by a reduction of stress in the layer due to a volume decrease associated with the grain formation. X-ray line broadening analysis delivers an average grain size in the layer of $\sim 53.9$ nm.

Increasing the curing temperature to 900 and 1200 °C results in phase transformation. The anatase phase is transformed to the rutile phase upon increasing the curing temperature. The resulting film is a mixture of anatase and rutile.[16] This effect is seen from the diffractograms in Fig. 2, which show a rutile reflection for both the 900 and 1200 °C cured specimens. X-ray line broadening analysis delivers for the 900 and 1200 °C specimens average grain sizes of $\sim 99.3$ nm and $\sim 173.3$ nm, respectively. The average grain sizes correspond to those obtained using scanning electron microscopy. In the derivation of the average grain sizes from x-ray line broadening, the contribution of second and third order stresses to the broadening is neglected. Because the determined grain sizes correspond well to the scanning electron microscope values, the second and third order stresses are assumed to be small enough to not influence the line profiles.

The measured residual stresses in the layers increase with the curing temperature. Together with the fact that the stresses measured are tensile, this may be an indication that the residual stress state is evolved upon *cooling* during the curing process. The linear thermal expansion coefficient of the layers and the substrate are $\sim (8.0 \pm 0.5)10^{-6}\ K^{-1}$ and $\sim (0.5 \pm 0.1)10^{-6}\ K^{-1}$, respectively.[17,18] From the difference in thermal expansion coefficients and the temperature difference upon cooling from curing temperature to room temperature, a thermally induced stress may be calculated according to[19]

$$\sigma_{\text{thermal}} = \frac{E_l}{1 - \nu_l} \int_{T_R}^{T_C} \Delta\alpha\, dT \tag{8}$$

In this equation, $\Delta\alpha$ is the difference in thermal expansion coefficients, $\Delta T$ is the temperature difference, $E_l$ is Young's modulus of the layer, and $\nu_l$ its Poisson's ratio. In this equation, the substrate is assumed to be infinitely stiff. Using this expression, the thermally induced stress in the layers are estimated as listed in Table VI.

In Fig. 8 the measured residual stress values as well as the calculated thermal misfit induced stresses are plotted versus the curing temperature of the specimen. From the graph it is suggested that the measured residual stress values lie within the expected range for thermal misfit induced stresses in the layer.

If the stresses, however, are not solely due to thermal misfit, then a line may be fitted through the data which is not forced to go through the origin of the graph, the fitted line then intersects the vertical axis at $\sim 300$ MPa. This effect may be an indication that the densification stress upon curing of the specimen is $\sim 300$ MPa. The main assumption made in this conclusion is that the densification in the three different layers cured at 700, 900, and 1200 °C is comparable. If the densification differs for the various curing temperatures, then the densification shrinkage will cause different densification stresses in the various cured layers. The offset in the residual stress versus temperature line will then be nonequal for different curing temperatures; hence, fitting a straight line through the points, indicating that the differences in stresses is solely due to thermal misfit, is no longer justified.

Overall it is seen that large stresses may evolve in the curing process, which may be attributed to the differences in thermal expansion coefficients. It has to be emphasized that measured stress state is explained from the difference in expansion coefficients during the *cooling* process, meaning that the stress present in specimen at the curing temperature is taken as the reference state. During the heating process it is suggested that the stress generated by capillary forces in the starting material is substantially reduced. The stress after a *complete* thermal cycle of heating up and cooling down is assumed to be due to the differential shrinkage of the layer and substrate.

TABLE VI. Thermally induced stress.

| Curing temperature (°C) | $\sigma_{th}$ (GPa) |
|---|---|
| 700 | 1.3 ± 0.4 |
| 900 | 1.6 ± 0.5 |
| 1200 | 2.1 ± 0.6 |

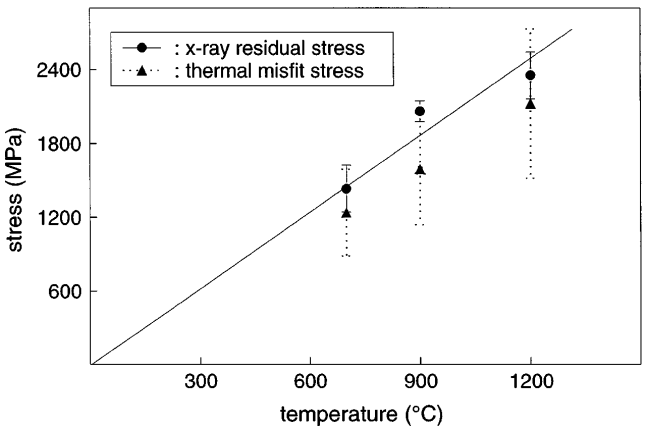


FIG. 8. Determined residual stresses in the various furnace-cured $TiO_2$ specimens. In the graph, the calculated thermal stress is also depicted.

## REFERENCES


1. Y. Ohya, H. Saiki, T. Tanaka, and Y. Takahashi, J. Am. Ceram. Soc. **79**, 825 (1996).
2. C. J. Brinker and G. W. Scherrer, *Sol-Gel Science* (Academic Press, San Diego, CA, 1990).
3. F. van Looyengoed, Thesis, Rijksuniversiteit Groningen (1996), p. 19.
4. B. D. Cullity, *Elements of X-ray Diffraction* (Addison-Wesley, Reading, MA, 1978), p. 447.
5. I. A. Montoya, T. Viveros, J. M. Dominguez, L. A. Canales, and I. Schifter, Catal. Lett. **15**, 207 (1992).
6. Y. Takahashi and Y. Matsuoka, J. Mater. Sci. **23**, 225 (1988).
7. D. Bersani, R. Capelletti, P. P. Lottici, G. Gnappi, and A. Montenero, Mater. Sci. Forum **239**, 87 (1997).
8. I. Manzini, G. Antonioli, D. Bersani, P. P. Lottici, G. Gnappi, and A. Montenero, J. Non-Cryst. Solids **192**, 519 (1995).
9. B. E. Warren, *X-ray Diffraction* (Addison-Wesley, Reading, MA, 1969), p. 253.
10. L. J. M. G. Dortmans, R. Morell, and G. de With, J. Eur. Ceram. Soc. **12**, 205 (1993).
11. E. E. Underwood, *Quantitative Stereology* (Addison-Wesley, Reading, MA, 1970).
12. L. C. Stearns and M. P. Harmer, J. Am. Ceram. Soc. **79**, 3013 (1996).
13. I. C. Noyan and J. B. Cohen, *Residual Stress, Measurements by Diffraction and Interpretation* (Springer-Verlag, New York, 1987), p. 119.
14. B. E. Yoldas, Appl. Opt. **21**, 2960 (1982).
15. B. E. Yoldas, J. Sol-Gel Sci. Technol. **1**, 65 (1993).
16. N. J. Hess and G. J. Exarhos, in *Thin Films: Stresses and Mechanical Properties V*, edited by S. P. Baker, P. Børgesen, P. H. Townsend, C. A. Ross, and C. A. Volkert (Mater. Res. Soc. Symp. Proc. **356**, Pittsburgh, PA, 1995), p. 597.
17. M. F. Ashby, Cambridge Materials Selector (1993).
18. Anon., *Engineered Materials Handbook, Vol. 4, Ceramics and Glasses* (ASM INTERNATIONAL, Materials Park, OH, 1991), p. 755.
19. G. Dreier and S. Schmauder, Scripta Metall. Mater. **28**, 103 (1993).